Special Feature: Dynamics Modeling Supporting Vehicle Performance

Research Report

Study on Direct Yaw Moment and Power Consumption of an In-wheel Motor Vehicle

Takao Kobayashi, Etsuo Katsuyama, Hideki Sugiura, Eiichi Ono and Masaki Yamamoto

Report received on Jul. 20, 2016

ABSTRACT The present paper clarifies the effect of direct yaw moment control on power consumption using in-wheel motors in steady-state cornering. The key idea is the formulation of cornering resistance from the standpoint of the direct yaw moment. The formulation results for cornering resistance and power consumption were validated through actual vehicle tests. The simulation model revealed that direct yaw moment control can be realized with little additional power, provided that both the inner and outer driving forces act in the same direction. Furthermore, the model can be used to compare typical direct yaw moment controls in terms of power consumption characteristics. The present paper also discusses the energy equilibrium mechanism whereby input power to the tire is dissipated at the tire contact patch. This fundamental knowledge is helpful for developing efficient cornering control methods.

KEYWORDS Vehicle Dynamics, In-wheel Motor, Direct Yaw Moment, Energy Management

1. Introduction

The electrification of automotive powertrain systems is a focus of increasing attention as a means of helping to resolve the issues of global warming, because electric automotive powertrain systems have a lower environmental load compared to internal combustion engines. In addition, independent installation of electric motors enables more flexible vehicle packaging and driving force distribution control. The electric motor installed inside each wheel is called an in-wheel motor, and a vehicle equipped with in-wheel motors is expected as a future electric vehicle.

In the past, various driving force distribution controls have been studied in terms of vehicle maneuverability and safety.(1-4) However, since the improvement of the miles per charge is necessary in order to broaden the use of electric vehicles, the additional power required to achieve vehicle dynamics control and the possibility of optimizing the cornering efficiency should be clarified. Although some reports(5-7) have developed control methods to reduce energy consumption while turning, the energy loss mechanism due to turning has not yet been formulated. Therefore, in order to clarify the cornering loss and realize efficient direct yaw moment control (DYC), as a first step, the present paper describes the formulation of power consumption in steady-state cornering. Validation tests are conducted using an actual vehicle equipped with in-wheel motors.

2. Simulation Model

2. 1 Driving Resistance while Turning

In the present paper, a linear two-wheel model is used to formulate the driving resistance while turning, as shown in **Fig. 1**. The equations of motion are expressed as follows:

Longitudinal:

$$m\left(\dot{u}-vr\right)=F_x-F_{rr}-F_{ar}-2F_{yf}\sin\delta_f-2F_{yr}\sin\delta_r\,, \quad (1)$$

Lateral:

$$m\left(\dot{v}+ur\right)=2F_{yf}\cos\delta_f+2F_{yr}\cos\delta_r\,, \quad (2)$$

Yaw:

$$I_z\dot{r}=2l_fF_{yf}\cos\delta_f-2l_rF_{yr}\cos\delta_r+M_z\,. \quad (3)$$

In the above equations, m is the vehicle mass, I_z is the yaw inertia, l_f and l_r are the distances from the gravity center to the front and rear axles, respectively, δ_f and δ_r are the front and rear actual steer angles, respectively, u and v are the longitudinal and lateral velocities, respectively, r is the yaw rate, F_x is the total driving force, F_{yf} and F_{yr} are the front and rear lateral forces, respectively, and M_z is the direct yaw moment. The rolling resistance F_{rr} and aerodynamic resistance F_{ar} are expressed as follows:

$$F_{rr} = \mu_r mg, \quad F_{ar} = \rho A C_D V^2/2 , \tag{4}$$

where μ_r is the rolling resistance coefficient, g is gravitational acceleration, ρ is the air density, A is the frontal projected area, C_D is the aerodynamic resistance coefficient, and V is the vehicle velocity, which is equal to the longitudinal velocity u.

In steady-state cornering and linear conditions, the total driving force can be obtained by substituting the following equations into the equations of motion:

$$\dot{u} = 0, \quad \dot{v} = 0, \quad \dot{r} = 0 ,$$

$$u = V\cos\beta \approx V, \quad v = V\sin\beta \approx V\beta ,$$

$$\cos\delta_f \approx 1, \quad \cos\delta_r \approx 1 ,$$

$$\sin\delta_f \approx \delta_f , \quad \sin\delta_r \approx \delta_r , \tag{5}$$

where β is the body slip angle.

The total driving force is given by

$$F_x = F_{rr} + F_{ar} + 2F_{yf}\left(\delta_f - \beta\right) + 2F_{yr}\left(\delta_r - \beta\right) . \tag{6}$$

In the present paper, we define the cornering resistance as follows:

$$F_{cr} \equiv 2F_{yf}\left(\delta_f - \beta\right) + 2F_{yr}\left(\delta_r - \beta\right) . \tag{7}$$

Equation (7) indicates that the cornering resistance interferes with the vehicle longitudinal motion due to the front and rear lateral forces.

Then, the respective front and rear steer angles and body slip angle can be expressed as follows, using the linear two-wheel model:

$$\delta_f - \delta_r = \left(1 - \frac{m}{2l^2}\frac{l_f K_f - l_r K_r}{K_f K_r}V^2\right)\frac{l}{R} - \frac{K_f + K_r}{2lK_f K_r}M_z , \tag{8}$$

$$\beta = \frac{1}{1 - \dfrac{m}{2l^2}\dfrac{l_f K_f - l_r K_r}{K_f K_r}V^2} \begin{bmatrix} \left(1 - \dfrac{m}{2l}\dfrac{l_f V^2}{l_r K_r}\right)\dfrac{l_r}{l}\delta_f + \left(1 + \dfrac{m}{2l}\dfrac{l_r V^2}{l_f K_f}\right)\dfrac{l_f}{l}\delta_r \\ -\dfrac{mV^2 + 2\left(l_f K_f - l_r K_r\right)}{4l^2 K_f K_r}M_z \end{bmatrix} , \tag{9}$$

where A_y is the lateral acceleration, K_f and K_r are the front and rear cornering stiffnesses of the tires, respectively, and l is the wheelbase. Using Eqs. (8) and (9), the cornering resistance can be obtained again as follows:

$$F_{cr} = \left(\frac{l_r^2}{K_f} + \frac{l_f^2}{K_r}\right)\frac{\left(mA_y\right)^2}{2l^2} - \left[\frac{1}{R} + \left(\frac{l_r}{K_f} - \frac{l_f}{K_r}\right)\frac{mA_y}{l^2}\right]M_z + \left(\frac{1}{K_f} + \frac{1}{K_r}\right)\frac{M_z^2}{2l^2} . \tag{10}$$

The first term in Eq. (10) indicates that the cornering resistance increases with lateral acceleration and that higher cornering stiffness is desirable. The second term indicates that the direct yaw moment can reduce the cornering resistance greatly if the cornering radius is small and the difference between the front and rear tire cornering stiffnesses is large. The third term indicates that a higher cornering stiffness can suppress the increase in the cornering resistance caused by the direct yaw moment.

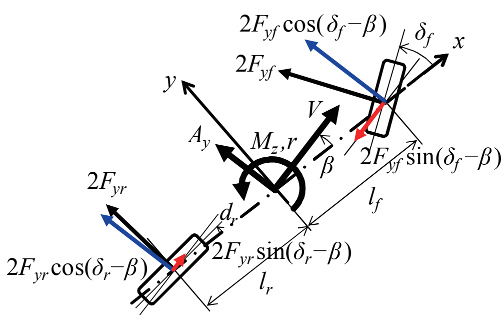

Fig. 1 Two-wheel vehicle model.

2. 2 Power Consumption while Turning

The total mechanical power P_v can be expressed as follows:

$$P_v = \sum_{j=1}^{4} \tau_j \omega_j . \tag{11}$$

Here, the driving torque and angular velocity of each wheel are represented as τ_j and ω_j, respectively (j = 1: front left, 2: front right, 3: rear left, 4: rear right). Assuming that the direct yaw moment is generated by the driving force difference between the inner and outer wheels, each driving torque can be expressed as follows:

$$\tau_j = \begin{cases} r_t\left(\dfrac{F_x}{4} - \dfrac{M_z}{2t}\right) \equiv r_t F_{xi} & (j = 1,3) \\ r_t\left(\dfrac{F_x}{4} + \dfrac{M_z}{2t}\right) \equiv r_t F_{xo} & (j = 2,4) \end{cases}, \tag{12}$$

where r_t is the tire radius, t is the track, and F_{xi} and F_{xo} are the driving forces at the inner and outer wheels, respectively. Regarding the angular velocities, we herein consider the effect of the longitudinal tire slip s_j, which is defined as follows:

$$s_j = \frac{F_{xj}}{K_{xj}} = -\frac{V_j - r_t\omega_j}{V_j}, \tag{13}$$

where K_{xj} is the driving stiffness and V_j is the vehicle speed in the tire position, as shown in the following equation, in terms of the vehicle speeds at the inner and outer wheels as V_i and V_o, respectively.

$$V_j = \begin{cases} V - \dfrac{t}{2}r \equiv V_i & (j = 1,3) \\ V + \dfrac{t}{2}r \equiv V_o & (j = 2,4) \end{cases} \tag{14}$$

Thus, the angular velocity can be expressed in terms of the longitudinal tire slip as follows:

$$\omega_j = \begin{cases} (1+s_i)\dfrac{V_i}{r_t} & (j = 1,3) \\ (1+s_o)\dfrac{V_o}{r_t} & (j = 2,4) \end{cases}, \tag{15}$$

where s_i and s_o are the longitudinal tire slips at the inner and outer wheels, respectively. By substituting Eqs. (12) through (15) into Eq. (11), the total mechanical power can be expressed as follows:

$$\begin{aligned} P_v &= F_{rr}V + F_{ar}V + 2(s_iF_{xi}V_i + s_oF_{xo}V_o) + \left(F_{cr} + \frac{M_z}{R}\right)V \\ &\equiv P_{rr} + P_{ar} + P_{sx} + P_{sy}\,. \end{aligned} \tag{16}$$

In the above equation, the power of the rolling resistance, aerodynamic resistance, cornering resistance, and longitudinal tire slip are denoted as P_{rr}, P_{ar}, P_{sx}, and P_{sy}, respectively. By substituting Eq. (10) into Eq. (16), the power of the cornering resistance can be obtained as follows:

$$\begin{aligned} P_{sy} &= \left(F_{cr} + \frac{M_z}{R}\right)V \\ &= \left[\begin{aligned} &\left(\frac{l_r^2}{K_f} + \frac{l_f^2}{K_r}\right)\frac{(mA_y)^2}{2l^2} - \left(\frac{l_r}{K_f} - \frac{l_f}{K_r}\right)\frac{mA_y}{l^2}M_z \\ &+ \left(\frac{1}{K_f} + \frac{1}{K_r}\right)\frac{M_z^2}{2l^2} \end{aligned}\right]V\,. \end{aligned} \tag{17}$$

As indicated by the second term in Eq. (17), unlike the cornering resistance, the reduction effect of the cornering resistance cancels out the additional power caused by the direct yaw moment, with the result that the reduction effect of the power depends only on the difference between the front and rear tire cornering stiffnesses. The other terms are the same as for the cornering resistance. If a large yaw moment is added, the longitudinal tire slip power increases and the difference between the inner and outer longitudinal slips increases.

2. 3 Mechanical Resistance of the Reduction Gear

In the in-wheel motor unit of the test vehicle, the motor torque is transmitted to the wheel through a counter gear and planetary gear. Therefore, by adding the mechanical resistance of the reduction gear to the driving resistance, the motor torque τ_{mj} can be expressed as follows:

$$\tau_{mj} = \begin{cases} \tau_j / i_g\eta_g & (\tau_{mj} > 0) \\ \eta_g\tau_j / i_g & (\tau_{mj} < 0) \end{cases}, \tag{18}$$

where i_g is the reduction gear ratio, and η_g is the transmission efficiency. We herein assume an efficiency of 96%, due to gear mesh loss. Then, the mechanical loss torque and force at the wheel can be expressed as follows:

$$\tau_{lj} = \begin{cases} i_g\tau_{mj} - \tau_j = (\eta_g^{-1} - 1)\tau_j & (\tau_{mj} > 0) \\ \tau_j - i_g\tau_{mj} = (\eta_g - 1)\tau_j & (\tau_{mj} < 0) \end{cases}, \tag{19}$$

$$F_{lj} = \frac{\tau_{lj}}{r_t} = \begin{cases} (\eta_g^{-1} - 1)F_{xj} & (F_{xj} > 0) \\ (\eta_g - 1)F_{xj} & (F_{xj} < 0) \end{cases}. \tag{20}$$

Then, the mechanical loss of the reduction gear can be obtained as follows:

$$L_{mj} = \tau_{lj}\omega_j = \begin{cases} \left(\eta_g^{-1} - 1\right)\tau_j\omega_j & \left(\tau_j > 0\right) \\ \left(\eta_g - 1\right)\tau_j\omega_j & \left(\tau_j < 0\right) \end{cases} . \tag{21}$$

Figure 2 shows the change in mechanical resistance caused by the driving force distribution. Although the mechanical resistance remains low at steady-state driving force F_{x0}, the mechanical resistance per wheel increases, provided that the inner and outer driving forces work in opposite directions. The mechanical loss has the same characteristics as the mechanical resistance.

2. 4 Electric Loss of the Motor and Inverter

An interior permanent magnet synchronous motor (IPMSM) model was constructed based on equivalent circuit theory,(8) as shown in **Fig. 3**. According to this theory, the equivalent circuit equations can be expressed as shown in the following equations:

$$i_{dj} = i_{odj} + i_{cdj}, \quad i_{qj} = i_{oqj} + i_{cqj} , \tag{22}$$

$$\begin{bmatrix} v_{dj} \\ v_{qj} \end{bmatrix} = R_a \begin{bmatrix} i_{odj} \\ i_{oqj} \end{bmatrix} + \left(1 + \frac{R_a}{R_c}\right) \begin{bmatrix} v_{odj} \\ v_{oqj} \end{bmatrix} + p \begin{bmatrix} L_d & 0 \\ 0 & L_q \end{bmatrix} \begin{bmatrix} i_{odj} \\ i_{oqj} \end{bmatrix}, \tag{23}$$

$$\begin{bmatrix} v_{odj} \\ v_{oqj} \end{bmatrix} = \begin{bmatrix} 0 & -\omega_{ej} L_q \\ \omega_{ej} L_d & 0 \end{bmatrix} \begin{bmatrix} i_{odj} \\ i_{oqj} \end{bmatrix} + \begin{bmatrix} 0 \\ \omega_{ej} \Psi_a \end{bmatrix}, \tag{24}$$

where i_d and i_q are the currents of the d-axis and q-axis, respectively, v_d and v_q are the voltages of the d-axis and q-axis, respectively, R_a is the coil resistance, R_c is the equivalent iron loss resistance, L_d and L_q are the d-axis and q-axis inductances, respectively, Ψ_a is the flux linkage, ω_e is the electrical angular velocity, and p is the differential operator. In the present paper, the parameters in the equivalent circuit model were identified through bench tests. By solving the above equations, the motor torque, copper loss L_{Cuj}, and iron loss L_{Fej} can be obtained as follows:

$$\tau_{mj} = P_n \left[\Psi_a i_{oqj} + \left(L_d - L_q\right) i_{odj} i_{oqj} \right] , \tag{25}$$

$$L_{Cuj} = R_a I_{aj}^{\ 2} = R_a \left(i_{dj}^{\ 2} + i_{qj}^{\ 2} \right) , \tag{26}$$

$$L_{Fej} = \frac{v_{odj}^{\ 2} + v_{oqj}^{\ 2}}{R_c} = \frac{\omega_{ej}^{\ 2} \left[\left(L_d i_{odj} + \Psi_a \right)^2 + \left(L_q i_{oqj} \right)^2 \right]}{R_c} , \tag{27}$$

where P_n is the number of pairs. For ease of calculation, we treat the inverter loss L_{Invj} as a simplified loss that is proportional to the current vector I_{aj}, as follows:

$$L_{Invj} = \kappa I_{aj} . \tag{28}$$

The total electric loss L_{ej} can be expressed as follows:

$$L_{ej} = L_{Cuj} + L_{Fej} + L_{Invj} . \tag{29}$$

Figure 4 shows the electric loss at a rotational speed corresponding to 40 km/h. The simulation results

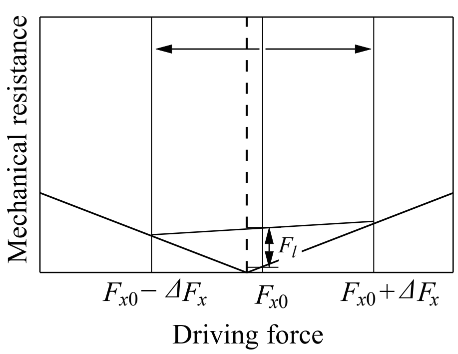

Fig. 2 Mechanical resistance characteristics.

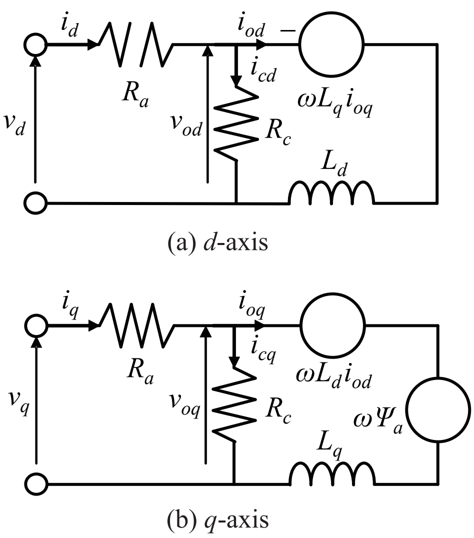

Fig. 3 Equivalent circuits of the IPMSM.

exhibit the same trend as the experimental results. Although the electric loss remains low at steady-state driving torque τ_0, the electric loss per wheel and the mechanical resistance increase at ΔL_0, provided that the inner and outer driving forces work in opposite directions.

3. Actual Vehicle Test Results

3. 1 Test Conditions

A passenger hybrid vehicle was customized to obtain a test vehicle equipped with four in-wheel motors. The original drive line was removed, and in-wheel motors were installed at each wheel. The major specifications are shown in **Table 1**.

Actual vehicle tests were conducted to validate the above formulations. For the sake of accuracy, the vehicle speed was controlled to be constant by a cruise control system and the steering angle was set to trace a constant radius circle on an asphalt road with a constant friction coefficient, μ.

First, the cornering resistance characteristics without the direct yaw moment were determined at 35 km/h. The effect of lateral acceleration was considered for circles of various turning radii.

Two experimental conditions were applied in order to consider the effect of the direct yaw moment: 20 km/h for a turning radius of 15 m (R15 m) and 40 km/h for a turning radius of 60 m (R60 m). For both conditions, the lateral acceleration was approximately 2 m/s^2. The applied direct yaw moment was changed each lap, and the motor torque command values, motor rotational speeds, inverter voltage, and current were measured.

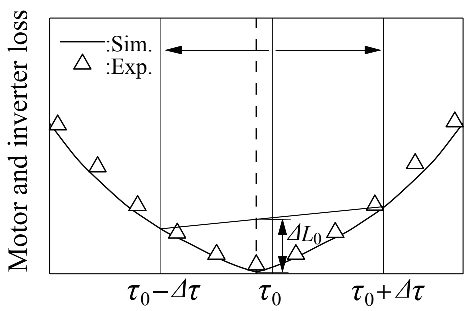

Fig. 4 Electric loss characteristics.

Table 1 Specifications of the test vehicle.

Vehicle mass	2,195 kg
Max. power	40 kW × 4
Max. torque at axle	550 Nm × 4
Max. vehicle speed	200 km/h

3. 2 Driving Resistance while Turning

The driving resistance was obtained as the total measured motor torque at each wheel, including the mechanical resistance of the reduction gears. In the present paper, we calculate the driving resistance by adding the mechanical resistance at each wheel to the driving resistance, as follows:

$$F_m = F_x + \sum_{j=1}^{4} F_{lj}\,. \tag{30}$$

Figure 5 compares the experimental and simulation results for the cornering resistance without the direct yaw moment. The lateral force saturates in the high lateral acceleration region, resulting in higher cornering resistance as compared to the linear simulation result. However, the simulation model can predict the resistance precisely in the low-lateral-acceleration region.

Figure 6 shows the experimental and simulation results for R15 m and R60 m, respectively. The figure shows the simulation results for the driving resistances at the motors and tires. The difference between these resistances is the mechanical resistance. As shown in Figs. 6(a) and (b), the simulation results exhibit the same trends as the experimental results. The most

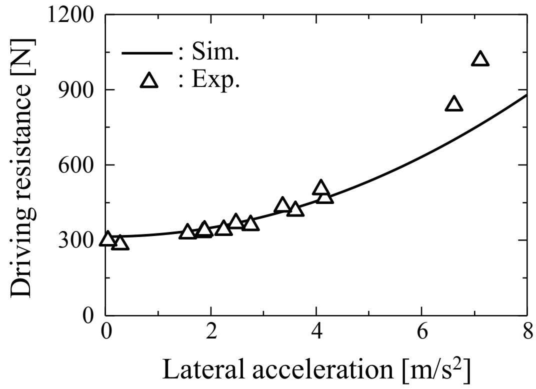

Fig. 5 Driving resistance in steady-state cornering.

significant point is that the driving resistance trend changes due to the cornering radius. As shown in Eq. (10), the reduction effect due to the direct yaw moment is inversely proportional to the cornering radius. Compared to the case of R60 m (Fig. 6(b)), the cornering radius of R15 m (Fig. 6(a)) is smaller and the cornering resistance decreases greatly. Although the mechanical resistance increases in the region where the inner wheels regenerate, the reduction effect at R15 m outweighs the increase in mechanical resistance. Note that a more accurate simulation can be achieved by considering the change in transmission efficiency in accordance with the operating point of the gear.

3. 3 Power Consumption while Turning

The total power consumption and mechanical power were obtained as the product of the measured inverter current and voltage and the product of the measured motor torque and rotational speed, respectively. The total mechanical power can be calculated by adding the mechanical loss at each wheel to the mechanical power as follows:

$$P_m = P_v + \sum_{j=1}^{4} L_{mj} \,. \tag{31}$$

The total power consumption can be calculated by adding the electric loss of each wheel to the total mechanical power as follows:

$$P_e = P_v + \sum_{j=1}^{4} L_{mj} + \sum_{j=1}^{4} L_{ej} \,. \tag{32}$$

Figure 7 shows the experimental and simulation results for R15 m and R60 m, respectively. The figure shows the power consumption and the mechanical power, the difference between which is the electric loss. As shown in Figs. 7(a) and (b), the simulation

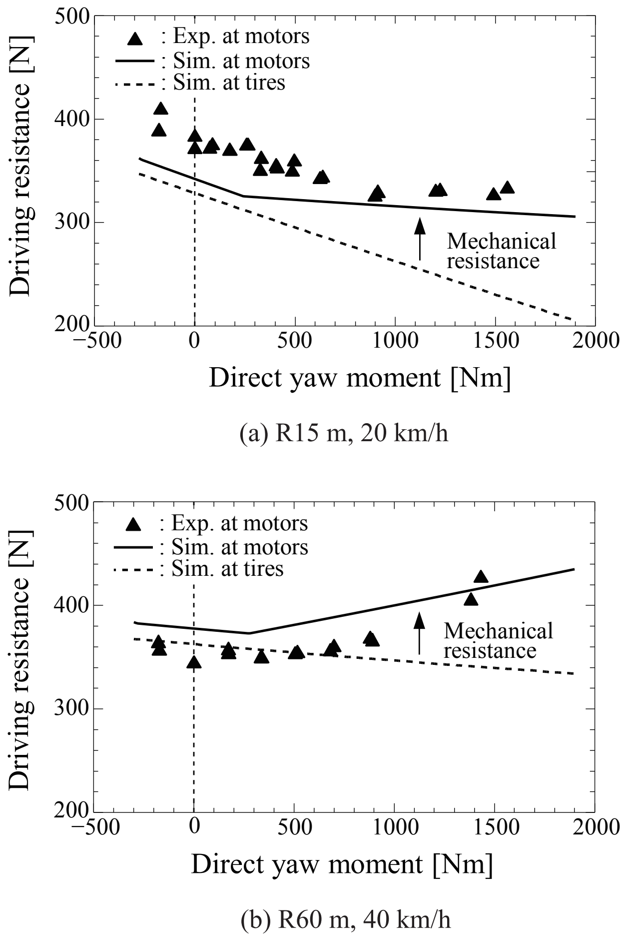

Fig. 6 Driving resistance vs. direct yaw moment.

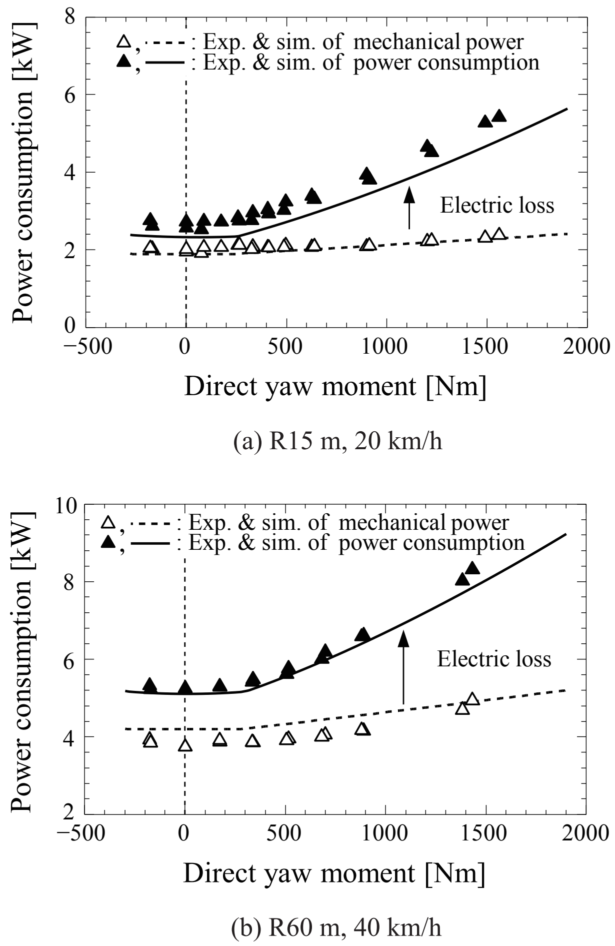

Fig. 7 Power consumption vs. direct yaw moment.

results exhibit the same trends as the experimental results. The power consumption and mechanical power exhibit similar trends between R15 m (Fig. 7(a)) and R60 m (Fig. 7(b)), regardless of the cornering radius. This is because the reduction effect of the mechanical power is not affected by the cornering radius, as shown in Eq. (17). In addition, since the test vehicle uses the same tires for the front and rear, the mechanical power is minimized without DYC. However, the mechanical power changes little due to the cornering resistance and longitudinal slip. As a result, DYC requires little additional power, provided that the inner and outer driving forces act in the same direction.

4. Considerations

4. 1 Power Consumption of Typical DYCs

As an application of the simulation model, the power consumption characteristics of typical DYCs were calculated. **Figures 8**(a) and (b) compare the required direct yaw moment and power consumption of neutral steering control, body slip angle control (β = 0), and load-proportional driving force control. The cornering radius was assumed to 100 m.

Neutral steering control cancels out the change in steer angle due to changes in vehicle velocity. As shown in Fig. 8(a), the required direct yaw moment increases with the vehicle velocity. As a result, the power consumption increases with the vehicle velocity, as shown in Fig. 8(b).

The body slip angle control zeroes the body slip angle. The slip angle changes from outward to inward at approximately 70 km/h, and the direct yaw moment changes from positive to negative. Except at the boundary velocity, significant power consumption is required to control the slip angle.

Load-proportional driving force control distributes the driving force in proportional to the vertical load, which spreads the work load equally between all wheels. As shown in Fig. 8(a), when the lateral acceleration increases with the vehicle velocity, the direct yaw moment increases slightly. As shown in Fig. 8(b), the power consumption increases in the higher direct yaw moment region. However, the additional power is small because load-proportional driving force control does not require regeneration of the inner wheel, even if the inner wheels lose traction. Thus, using the formulation results for the power consumption, the advantages and disadvantages of vehicle dynamics control can be calculated theoretically.

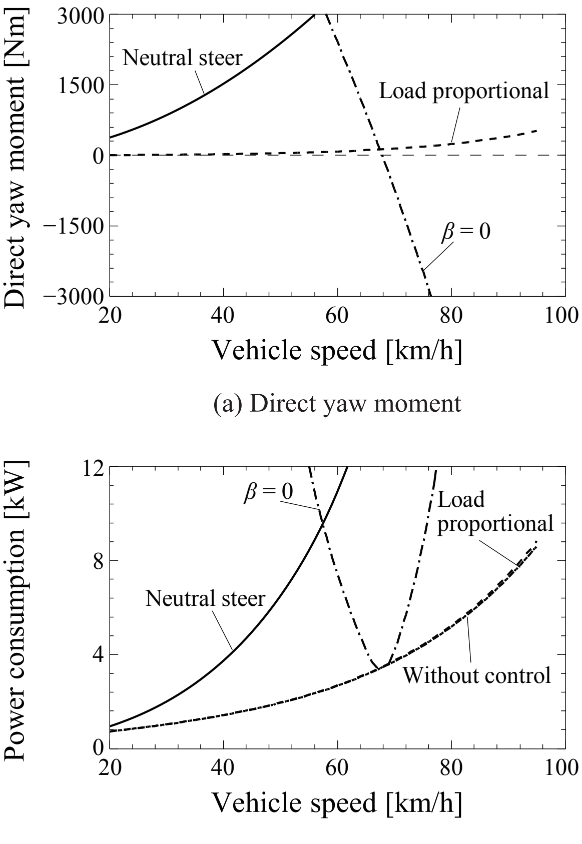

Fig. 8 Direct yaw moment and power consumption of typical DYCs.

4. 2 Tire Dissipation Power at the Contact Patch

This section describes the dissipation of cornering resistance and longitudinal slip. First, the cornering resistance and the other variables are re-formulated in terms of the front and rear tire slip angles α_f and α_r, respectively, as follows:

$$F_{yf} = -K_f \alpha_f, \quad F_{yr} = -K_r \alpha_r, \tag{33}$$

$$M_z = -2l_f F_{yf} + 2l_r F_{yr}, \tag{34}$$

$$\delta_f - \delta_r = \frac{l}{R} + \left(\alpha_r - \alpha_f\right), \tag{35}$$

$$\beta = \frac{l_r}{R} + \alpha_r + \delta_r \,. \tag{36}$$

By substituting Eqs. (33) through (36) into Eq. (7), the cornering resistance can be expressed as follows:

$$F_{cr} = 2K_f \alpha_f{}^2 + 2K_r \alpha_r{}^2 - \frac{M_z}{R} \,. \tag{37}$$

The first and second terms represent the local cornering resistances of the front and rear tires, respectively, and the third term represents the reduction effect by the direct yaw moment. Moreover, by substituting Eq. (37) into Eq. (17), the power of cornering resistance can be obtained as follows:

$$\begin{aligned} P_{sy} &= \left(2K_f \alpha_f{}^2 + 2K_r \alpha_r{}^2\right)V \\ &= -2\left(F_{yf}V_{syf} + F_{yr}V_{syr}\right), \end{aligned} \tag{38}$$

where V_{syf} and V_{syr} are the front and rear lateral slip velocities, respectively. Representing the inner and outer longitudinal slip velocities as V_{sxi} and V_{sxo}, the power of the longitudinal slip can be expressed as follows:

$$P_{sx} = -2\left(F_{xi}V_{xsi} + F_{xo}V_{xso}\right). \tag{39}$$

Using Eqs. (38) and (39), the mechanical power can be expressed as follows:

$$\begin{aligned} P_v &= \sum_{j=1}^{4} \tau_j \omega_j \\ &= P_{sx} + P_{sy} \\ &= -\sum_{j=1}^{4}\left(F_{xj}V_{sxj} + F_{yj}V_{syj}\right) \\ &= -\sum_{j=1}^{4} \vec{F}_j \cdot \vec{V}_{sj} \,. \end{aligned} \tag{40}$$

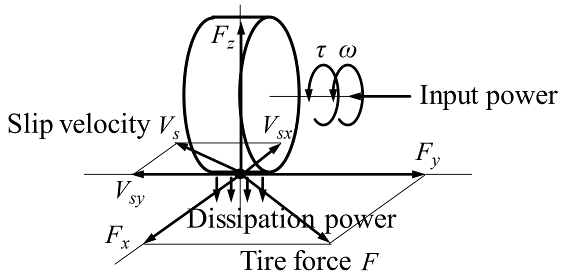

Fig. 9 Power dissipation at the tire contact patch.

From the above formulation, the mechanical power is equal to the scalar product of the tire force vectors and tire slip velocity vectors. This is assumed to be the power loss caused by the tire slip at the tire contact patch, which is eventually dissipated as heat(9-11) as shown in **Fig. 9**. Therefore, the reduction in power dissipation contributes to cornering efficiency.

5. Conclusion

In the present paper, we formulated the driving resistance and power consumption in steady-state cornering to clarify the cornering loss. Actual vehicle tests using a vehicle equipped in-wheel motors were conducted, and the obtained results validated the formulation results. The test results also clarified that the DYC can be realized with little additional power, provided that the inner and outer driving forces act in the same direction. In addition, the energy equilibrium state was explained theoretically such that the input power required to maintain steady-state cornering is dissipated at the tire contact patch.

Based on the formulation results, vehicle specifications and control methods that provide enhanced cornering efficiency will be proposed in the future.

References

(1) Mokhiamar, O. and Abe, M., "Effects of Optimum Cooperative Chassis Control from the Viewpoint of Tire Workload", *JSAE Trans.*, Vol. 35, No. 3 (2004), pp. 215-221.
(2) Ono, E., Hattori, Y., Muragishi, Y. and Koibuchi, K., "Vehicle Dynamics Integrated Control for Four-wheel-distributed Steering and Four-wheel-distributed Traction/braking Systems", *Vehicle System Dynamics*, Vol. 44, No. 2 (2006), pp. 139-151.
(3) Murata, S., "Innovation by In-wheel-motor Drive Unit", *Vehicle System Dynamics*, Vol. 50, No. 6 (2012), pp. 807-830.
(4) Katsuyama, E., "Decoupled 3D Moment Control Using In-wheel Motors", *Vehicle System Dynamics*, Vol. 51, No. 1 (2013), pp. 18-31.
(5) Abe, M., "Evaluation of Active Vehicle Motion Controls from Tire Energy Dissipation Points of View", *AVEC* (2012), 9p.
(6) Nishihara, O. and Higashino, S., "Optimum Distribution of Lateral and Traction/braking Forces for Energy Conservation", *Proc. 7th IFAC Symp. Advances Autom. Control* (2013).
(7) Yone, T. and Fujimoto, H., "Proposal of a Range Extension Control System with Arbitrary Steering

for In-wheel Motor Electric Vehicle with Four Wheel Steering", *Proc. 13th Int. Workshop Advanced Motion Control* (2014), pp. 363-373

(8) Morimoto, S., Takeda, Y. and Hirasa, T., "Parameter Measurement of PM Motor in dq Equivalent Circuit", *IEEJ Trans. Ind. Appl.* (in Japanese), Vol. 113, No. 11 (1993), pp. 1330-1331.

(9) Sorniotti, A., "Tire Thermal Model for Enhanced Vehicle Dynamics Simulation", *SAE Tech. Paper Ser.*, No. 2009-01-0441 (2009).

(10) Mizuno, M., Sakai, H., Oyama, K. and Isomura, Y., "Development of a Tyre Force Model Incorporating the Influence of the Tyre Surface Temperature", *Vehicle System Dynamics*, Vol. 43, Suppl. (2005), pp. 395-402.

(11) Hancock, M. J., Williams, R. A., Gordon, T. J. and Best, M. C., "A Comparison of Braking and Differential Control of Road Vehicle Yaw-sideslip Dynamics", *Proc. IMechE, Part D*, Vol. 219 (2005), pp. 309-327.

Figs. 1-4 and 6-9
Reprinted from Proc. FISITA World Autom. Congr. (2014), Paper No. F2014-IVC-005, Kobayashi, T., Katsuyama, E., Sugiura, H., Ono, E. and Yamamoto, M., Study on Driving Force Distribution and Power Consumption in Stedy State Cornering – Formulation and Validation Using In-wheel Motor Vehicle, © 2014 FISITA, with permission from FISITA.

Takao Kobayashi

Research Field:
- Vehicle Dynamics Control

Academic Society:
- Society of Automotive Engineers of Japan

Award:
- JSAE Ann. Congr. Autumn Best Presentation Award, 2012

Etsuo Katsuyama*

Research Field:
- Vehicle Dynamics Control

Academic Society:
- Society of Automotive Engineers of Japan

Awards:
- Best Paper Award, JSAE, 2013
- Arch T. Colwell Merit Award, SAE, 2014

Hideki Sugiura

Research Fields:
- Application of Multibody Dynamics
- Development of Suspension Design Method

Academic Societies:
- Society of Automotive Engineers of Japan
- The Japan Society of Mechanical Engineers

Awards:
- Certificate of Merit for Excellence in Design & Systems Contest, JSME, 2008 and 2011
- JSME Dynamics & Design Conference 2009 Best Presentation Award, 2010

Eiichi Ono

Research Field:
- Vehicle Dynamics Control

Academic Degree: Dr.Eng.

Academic Societies:
- The Japan Society of Mechanical Engineers
- Society of Automotive Engineers of Japan
- The Society of Instrument and Control Engineers

Awards:
- SICE Award for Outstanding Paper, 1995
- IFAC Congr. Appl. Paper Prize, 2002
- Paper Award of AVEC, 2002 and 2004
- JSME Medal for Outstanding Paper, 2007

Masaki Yamamoto*

Research Field:
- Vehicle Dynamics

Academic Degree: Dr.Eng.

Academic Societies:
- Society of Automotive Engineers of Japan
- The Japan Society of Mechanical Engineers

Awards:
- Asahara Award, JSAE, 1991
- Paper Award of AVEC, 2002
- ESV US Government Award, 2003
- Excellent Technical Paper Presentation Award, JSAE, 2015

* Toyota Motor Corporation